Supporting information

A Stable Narrow-Bandgap 2D Iron–Pyrazine Framework Exhibiting High Photoconductivity and Spin–Charge Coupling

Mohamed Saber Lassoued, Xue-Qi Huang, Abid Hussain, and Yan-Zhen Zheng*

School of Chemistry, Frontier Institute of Science and Technology, Interdisciplinary Research Center of Frontier Science and Technology, Xi'an Key Laboratory of Electronic Devices and Materials Chemistry, Xi'an Key Laboratory of Sustainable Energy and Materials Chemistry, Xi'an Jiaotong University, Xi'an 710054, China

E-mail: zheng.yanzhen@xjtu.edu.cn

CONTENTS

1. Materials

All reagents including lithium metal, 1,2-dihydroacenaphthylene (99%), anhydrous Fe_2O_3 (99.99%), pyrazine (≥99%), and anhydrous tetrahydrofuran (THF) were sourced from commercial suppliers and used as received. To prevent magnetic contamination, all reactions were stirred using Pyrex-glass-coated magnetic stir bars, and solids were handled exclusively with polypropylene or Pyrex spatulas.

2. Synthesis of (pyz)$FeCl_2$

All procedures related to the synthesis of (pyz)$FeCl_2$ were performed under ambient laboratory conditions. In a typical reaction, Fe_2O_3 (0.20 g, 1.6 mmol; Sigma-Aldrich, 99.99% trace metal basis), pyrazine (2.0 g, 25 mmol; Sigma-Aldrich, ≥99%), purified water (3 mL), and concentrated HCl (2 mL) were combined in a 50 mL Teflon-lined stainless-steel autoclave. The reactor was sealed and heated at 130 °C for 72 hours, then allowed to cool to room temperature. The resulting red microcrystalline solid was separated from the mother liquor by decantation, washed sequentially with N,N-dimethylformamide (20 mL) and acetonitrile (2 × 20 mL), and dried under vacuum to afford (pyz)$FeCl_2$ in 70–75% yield.

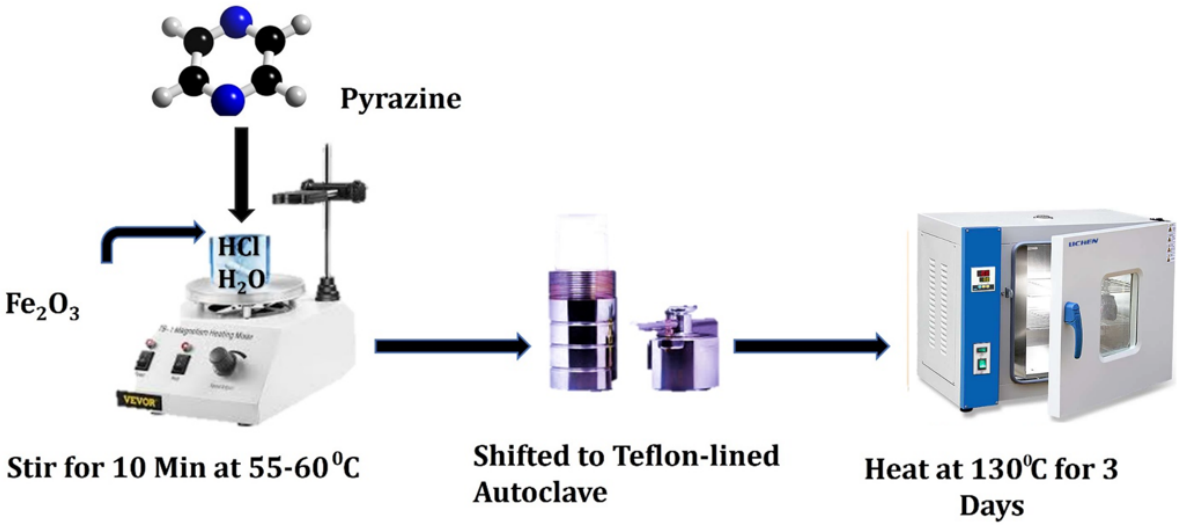

Scheme 1. Schematic illustration of the hydrothermal synthesis of (pyz)$FeCl_2$.

3. Characterization Methods and Simulation Details

3.1. Characterization Methods

X-ray Crystallographic Study

Single-crystal X-ray diffraction data for (pyz)$FeCl_2$ were acquired at 150 K on a Bruker SMART APEX II CCD diffractometer equipped with Mo Kα radiation (λ = 0.71073 Å), using a θ–ω scan mode. The structure was solved through direct methods and refined using full-matrix least-squares regression on F^2 via the SHELXTL package. [S1] All non-hydrogen atoms were modelled anisotropically. Full crystallographic parameters are summarized in Tables S1–S3. The Crystallographic Information File (CIF) has been deposited with the Cambridge Crystallographic Data Centre (CCDC) under accession number 2502909 and is available free of charge at: http://www.ccdc.cam.ac.uk/data_request/cif.

Powder X-ray Diffraction

Powder X-ray diffraction data were acquired using a Bruker D8 Advance diffractometer configured in θ–θ geometry. The instrument was equipped with a sealed-tube Cu Kα radiation source (λ = 1.5418 Å), Göbel mirror optics, and a LynxEye one-dimensional position-sensitive detector operating in Bragg–Brentano mode. Measurements were performed over a 2θ range of 2–50° with a step size of 0.02° and a counting time of 1 s per step.

Morphology and Elemental Composition

Scanning electron microscopy (SEM) imaging was performed using a KYKY EM-3200 field-emission microscope operated at an accelerating voltage of 25 kV. Prior to analysis, microcrystalline powder samples were gently ground, dispersed onto conductive carbon tape, and sputter-coated with a 5 nm Au/Pd layer to mitigate charging effects.

Elemental mapping and point analysis were conducted using an Oxford Instruments X-MaxN energy-dispersive X-ray spectrometer (EDS) attached to the same instrument. Measurements were acquired at 25 kV with a working distance of 8.5 mm and a live time of 60 s per point. Elemental quantification was carried out using the INCA software suite with ZAF correction, yielding semi-quantitative atomic percentages consistent with the expected Fe : Cl : N : C stoichiometry for (pyz)$FeCl_2$.

Optical Characterization

Solid-state UV-Vis-NIR diffuse reflectance spectra were acquired for pressed powder and thin-film samples using a Shimadzu UV-3600 spectrophotometer. $BaSO_4$ powder was

used as a reflectance standard. To minimize atmospheric oxidation, all spectra were collected within 10 minutes of sample sealing. Background correction was performed using an identically prepared empty sealed cell to subtract contributions from the sample holder and windows.

The reflectance data (R) were converted to Kubelka–Munk pseudo-absorbance values using the function $F(R) = (1 - R)^2 / 2R$ for subsequent band gap analysis. [S2, S3]

Thermogravimetric Analysis (TGA)

Thermal stability was evaluated using a Mettler–Toledo TGA/DSC 3+ Extreme simultaneous thermal analyzer. Finely ground samples (≈6–8 mg) were loaded into 70 μL alumina crucibles and heated from 298 K to 1073 K at a rate of 10 K·min^{-1} under a continuous flow of high-purity nitrogen (99.999%, 50 mL·min^{-1}, mass-flow-controlled). The microbalance was calibrated using certified indium and zinc standards prior to measurement, and baseline correction was performed using an empty crucible under identical conditions. Derivative thermogravimetry (DTG) and heat-flow signals were recorded simultaneously to differentiate between mass-loss steps and endothermic or exothermic events. Onset decomposition temperatures were determined via the extrapolated-baseline method, enabling accurate comparison with related hybrid materials.

Electrical Conductivity Measurements

Approximately 50 mg of (pyz)$FeCl_2$ powder was uniaxially cold-pressed under 5 tons into a pellet (10 mm diameter, ~0.30 mm thickness). Gold leads were attached to both faces using silver conductive paint (SPI Supplies) to form two-terminal contacts. The pellet was placed in a programmable oven and allowed to thermally equilibrate for 10 minutes at each temperature before measurement. A Keithley 2400 SourceMeter applied DC biases in the range of ±0.1–10 V, while the resulting current (nanoamperes to microamperes) was measured using a Keithley 6485 picoammeter connected in series. Current density (J) and electric field (E) were calculated as $J = I/S$ (where $S = 7.85 \times 10^{-3}$ cm^2) and $E = V/L$ (where $L = 0.03$ cm), respectively. The bulk conductivity (σ) was determined from the slope of the linear J–E curve as $\sigma = J/E$ at different temperatures.

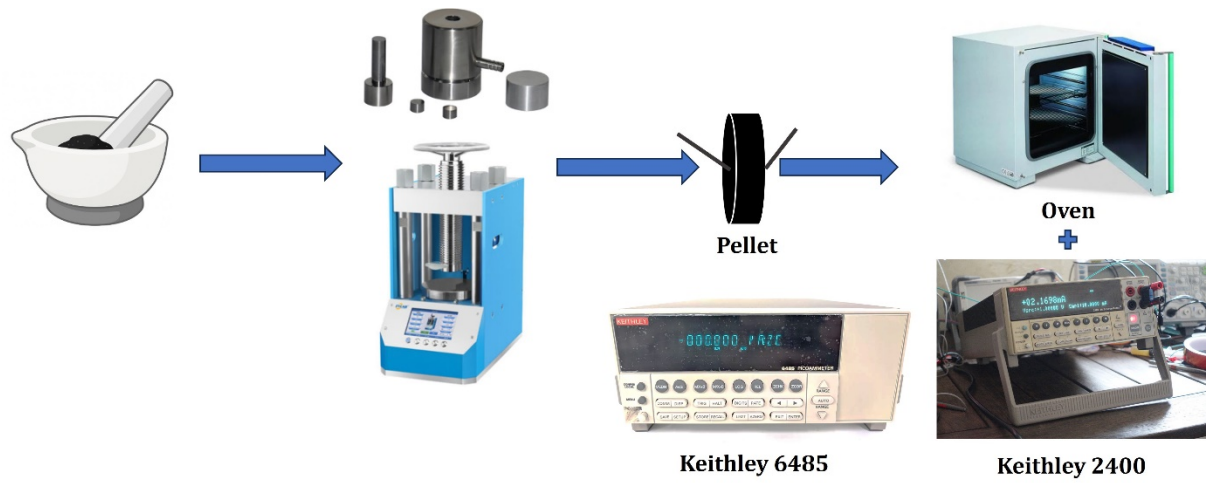

Scheme.2. Schematic illustration of pellet preparation and electrical measurement setup.

Photocurrent measurements.

Pellet was prepared by grinding 50–100 mg of polycrystalline (pyz)$FeCl_2$ into a homogeneous powder and pressing the material at 15 MPa for 10 minutes. Electrical contacts were made by applying conductive silver paste to two points on one face of each pellet. A narrow uncoated strip was intentionally left to allow direct illumination of the sample. Photocurrent responses were recorded using LED light sources at 365 nm and 600 nm. The light was alternately switched on and off every 40 s, and the corresponding current changes were monitored to evaluate the device's photoresponse.

X-ray Photoelectron Spectroscopy (XPS)

X-ray photoelectron spectroscopy (XPS) measurements were performed using a Thermo Scientific K-Alpha+ spectrometer equipped with a monochromated Al Kα X-ray source (hν = 1486.6 eV, 72 W, 15 kV). Powder samples of (pyz)$FeCl_2$ compound were pressed onto conductive indium foil and transferred into the instrument under ambient atmosphere. The analysis chamber was maintained at a base pressure below 2×10^{-9} mbar during measurements. Survey scans were collected using a pass energy of 200 eV and a step size of 1 eV. High-resolution spectra of the Fe 2p, N 1s, Cl 2p, and C 1s core-level regions were recorded with a pass energy of 50 eV and a step size of 0.1 eV. Each high-resolution scan was averaged over three consecutive sweeps to improve the signal-to-noise ratio.

Raman Spectroscopy

Raman spectra were acquired in backscattering geometry using a Horiba XploRA confocal Raman microscope equipped with a motorized XY stage, a 1200 grooves mm^{-1} grating, and a 50× Olympus long-working-distance objective (NA = 0.45). Pristine samples were sealed in quartz capillaries (0.5 mm inner diameter) and excited using a 785 nm diode laser with a power of 0.37 mW at the sample plane. Spectra were recorded with an integration time of 3 minutes, and two consecutive accumulations were averaged to enhance the signal-to-noise ratio.

Magnetic Characterization

DC magnetic properties were investigated with a Quantum Design Physical Property Measurement System (PPMS) equipped with a vibrating-sample magnetometer. Field dependent magnetisation (hysteresis) loops were measured between 2-300 K over the field range ±5 T to determine coercivity, remanence, and saturation magnetisation.

Stability Measurements

Freshly prepared (pyz)$FeCl_2$ powder was deposited onto clean glass substrates and placed in a sealed chamber containing a saturated aqueous solution of $Mg(NO_3)_2 \cdot 6H_2O$ to maintain a constant relative humidity of ~55%. [S4] To minimize unintended photochemical effects, the samples were stored in the dark throughout the duration of the experiment. The powder was not in direct contact with the salt solution. After 30 days of exposure under these controlled conditions, the phase stability of the sample was evaluated using powder X-ray diffraction (PXRD).

3.2 Simulation Details

All calculations in this work were performed using density functional theory (DFT) as implemented in the BIOVIA Materials Studio simulation package. [S5, S6] Electronic structure calculations employed the generalized gradient approximation (GGA) with the Perdew–Burke–Ernzerhof (PBE) functional. [S7, S8] A convergence threshold of 2×10^{-6} eV/atom was applied for the self-consistent field iterations. Ultrasoft pseudopotentials in the on-the-fly generation (OTFG) mode was used with a plane-wave energy cutoff of 489.8 eV. Band structure calculations for (pyz)$FeCl_2$ were performed both with and without spin–orbit coupling (SOC). In calculations without SOC, ultrasoft pseudopotentials and a kinetic energy cutoff of 260 eV were employed. For SOC-included

calculations, norm-conserving pseudopotentials and a kinetic energy cutoff of 600 eV were applied to ensure accuracy.

4. Hirshfeld Surface Analysis

The crystallization of the parent compound, (pyz)$FeCl_2$, is governed primarily by non-covalent interactions originating at the $FeCl_2$ inorganic nodes and propagating through the pyrazine-based organic pillars. Hirshfeld surface (HS) analysis (Fig.1h) offers a quantitative visualization of these interactions by mapping the normalized contact distance, dnorm, derived from internal (di) and external (de) distances to neighboring atoms. On the color-mapped HS surfaces, close contacts (shorter than the sum of van der Waals radii) appear as intense red regions, near vdW-distance contacts as white, and longer contacts as blue.

Complementary two-dimensional fingerprint plots (Fig. 1i and S3) indicate that interactions involving hydrogen dominate the crystal packing of the unreduced framework. H···Cl contacts constitute 31.8% of all surface interactions, followed by H···H (17.4%), Fe···N (12.5%), and N···H (9.3%), cumulatively accounting for ≈71% of hydrogen-involved contacts. The remaining 29% comprises weaker interactions, including C···C, Cl···Cl, and other van der Waals contacts, grouped as “Others” in the summary pie chart (Fig. S3).

Void analysis was performed using Crystal Explorer 21.5 to evaluate the packing efficiency and intermolecular interactions within the crystal lattice. The calculations were carried out in probe mode with a probe radius of 1.2 Å, a grid spacing/resolution of 0.1 Å, and the default surface/volume calculation settings of the program. The resulting visualization of the void regions provides insight into the accessible intermolecular spaces, packing compactness, and potential porosity of the structures. All reported void volumes and percentages were obtained directly from the Crystal Explorer analysis.

5. Supporting Tables and Figures

Table S1. Crystal data and structure refinement for (pyz)$FeCl_2$.

Compound	(pyz)$FeCl_2$
Empirical formula	C_4 H_4 Cl_2 N_2 Fe
Formula weight	206.84
Crystal dimensions (mm)	0.28*0.25*0.22
Crystal system	Orthorhombic
Space group	*C mmm*
a/Å	12.015(3)
b/Å	7.2065(14)
c/Å	3.5729(8)
α/°	90
β/°	90
γ/°	90
Volume/$Å^3$	309.36(12)
Z	2
ρ calcg/cm^3	2.220
μ /mm^{-1}	3.190
F(000)	204.0
h, k, l max	14, 8, 4
Data Completeness	98.00%
Data/restraints/parameters	169/0/18
Goodness-of-fit on F^2	1.42
Weight	$w = 1/[\sigma^2(F_o^2) + (0P)^2 + 8.0219P]$ where $P = (F_o^2 + 2F_c^2)/3$
	R $[F^2 > 2\sigma(F2)] = 0.06$ $R_{int} = 0.146$, $wR_2 = 0.159$
CCDC Number	2502909

Table S2. Summary of selected bond lengths (Å) and bond angles (°) of (pyz)$FeCl_2$

Bonds	**Length /Å**	**Bond pair**	**Angles /**
Fe1—Cl1^{i}	2.489 (2)	Cl1^{i}—Fe1—Cl1^{ii}	180
Fe1—Cl1	2.489 (2)	Cl1^{ii}—Fe1—Cl1	88.26 (11)
Fe1—Cl1^{ii}	2.489 (2)	Cl1^{i}—Fe1—Cl1	91.74 (11)
Fe1—Cl1^{iii}	2.489 (2)	Cl1^{i}—Fe1—Cl1^{iii}	88.26 (11)
Fe1—N1^{iii}	2.214 (12)	Cl1—Fe1—Cl1^{iii}	180
Fe1—N1	2.214 (12)	Cl1^{ii}—Fe1—Cl1^{iii}	91.74 (11)
Cl1—Fe1^{iv}	2.489 (2)	N1^{iii}—Fe1—Cl1^{ii}	90
N1—C1^{v}	1.331 (12)	N1—Fe1—Cl1^{i}	90
N1—C1	1.331 (12)	N1—Fe1—Cl1^{iii}	90
C1—C1^{vi}	1.38 (2)	N1—Fe1—Cl1^{ii}	90
C1—H1	0.9217	N1^{iii}—Fe1—Cl1^{i}	90
		N1^{iii}—Fe1—Cl1	90
		N1—Fe1—Cl1	90
		N1^{iii}—Fe1—Cl1^{iii}	90
		N1^{iii}—Fe1—N1	180
		Fe1^{iv}—Cl1—Fe1	91.74 (11)
		C1^{v}—N1—Fe1	121.7 (6)
		C1—N1—Fe1	121.7 (6)
		C1—N1—C1^{v}	116.6 (13)
		N1—C1—C1vi	121.7 (6)
		N1—C1—H1	118.7
		C1^{vi}—C1—H1	119.6

Symmetry codes: (i) x, y, z−1; (ii) −x+1, −y+1, −z; (iii) −x+1, −y+1, −z−1; (iv) x, y, z+1; (v) −x+1, y, z; (vi) x, −y+2, −z−1.

Table S3. Potential hydrogen bonding data of compound (pyz)$FeCl_2$

D-H	d(D-H)	d(H..A)	<DHA	d(D..A)	A	
C1-H1	0.93	2.948	127.14	3.587	Cl1	[x-1/2, y-1/2, z]

Table S4. Comparison of photodetectors performances for (pyz)$FeCl_2$ with others reported systems

Compounds	Dim	Voltage(V)	I_{light}(nA)	R(μA/W)	Ref
$\{Pb^{II}_2I_6[Pb^{II}(TETA)]\}_n$	2D	0.7	636	7.04	[S9]
$\{Pb^{II}_3I_8[Pb^{II}(TETA)]\}_n$	2D	0.7	780	8.457	[S9]
PDBI	0D	1	194	1.14	[S10]
$[Zn(TBAPy)_{1/2}(H_2O)_2]$	3D	0	$0.44*10^3$	-	[S11]
$(I\text{-}BA)_2(MA)_2Pb_3I_{10}$	2D	30	1000	12.78	[S12]
$(BBA)_2(MA)Pb_2I_7$	2D	10	1370	$3.8*10^4$	[S13]
$(C_4H_9NH_3)_2PbI_4$	2D	30	1	$3*10^3$	[S14]
$(C_4H_9NH_3)_2PbBr_4$	2D	0.5	-	$2.1*10^8$	[S15]
$\{(Pb_4Cl_2)(ndc)_4\cdot[(CH_3)_3NH]_2\}_n$	1D	-	380	-	[S16]
$\{[Pb(cbpy)_2](I_3)_4\cdot I_2\}_n$	2D	0.5	2600	-	[S17]
(pyz)$FeCl_2$	**2D**	**5**	**18000**	**67.8**	**This work**

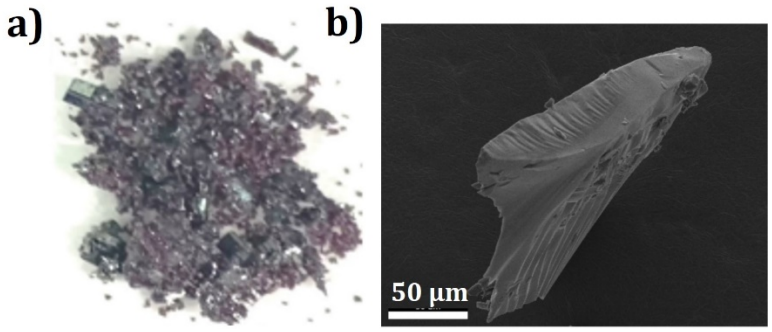

Figure S1. (a) The crystal images of (pyz)$FeCl_2$. (b) SEM image of a (pyz)$FeCl_2$ single crystal

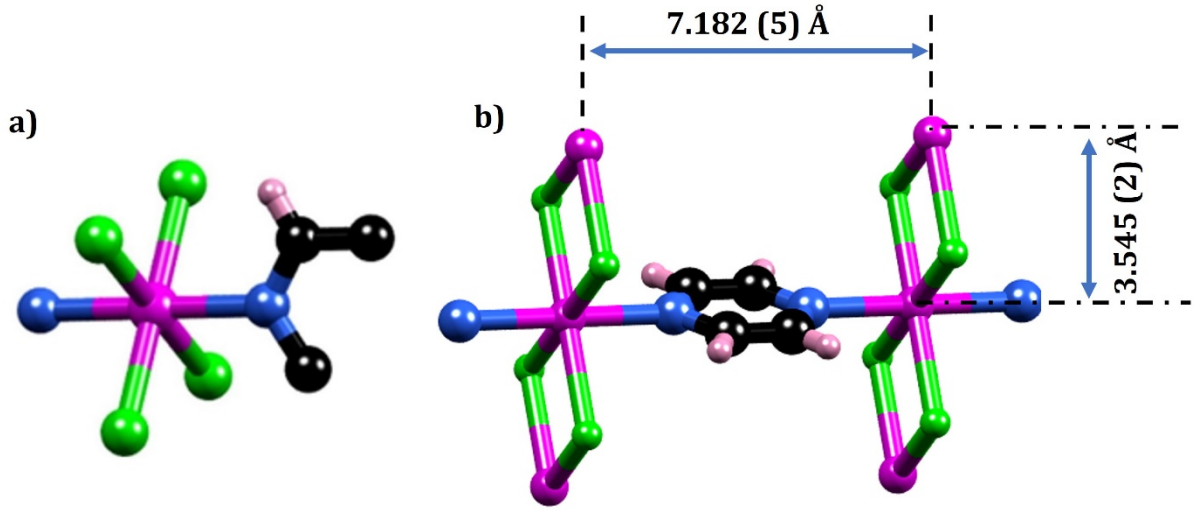

Figure S2. (a) Asymmetric unit of (pyz)$FeCl_2$. Crystal Structure of (pyz)$FeCl_2$ Highlighting Key Interatomic Fe···Fe Distances

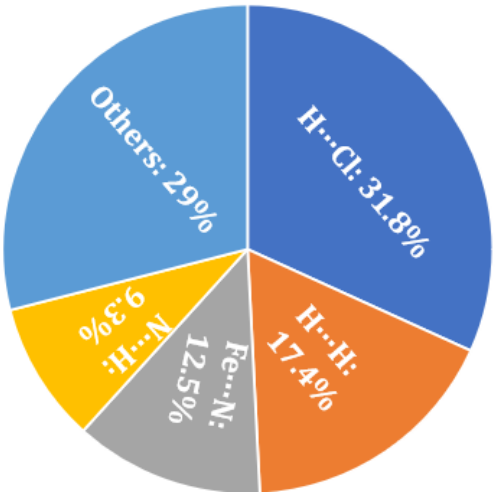

Figure S3. Different Hirshfeld surface interactions of (pyz)$FeCl_2$

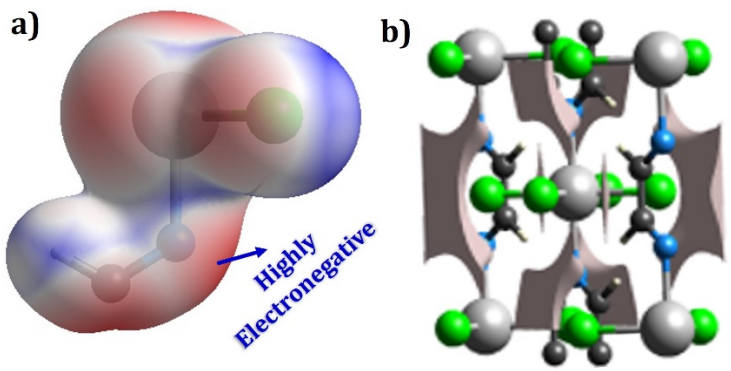

Figure S4. Electron density map of **(pyz)$FeCl_2$**. (k) Crystal voids of **(pyz)$FeCl_2$.**

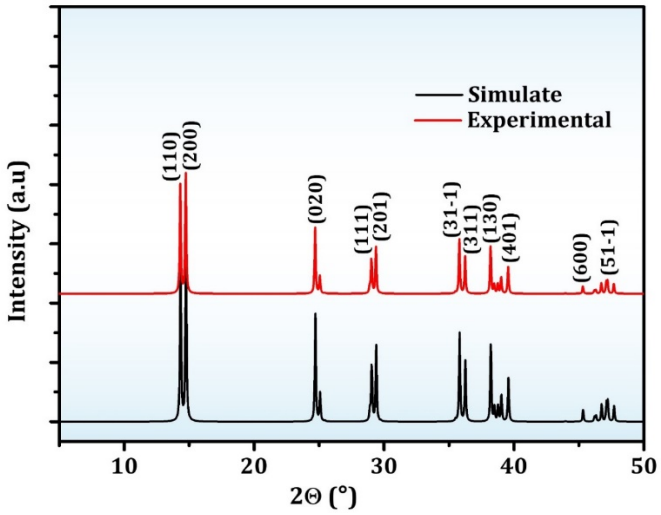

Figure S5. Experimental PXRD pattern of (pyz)$FeCl_2$ in comparison to its simulation pattern

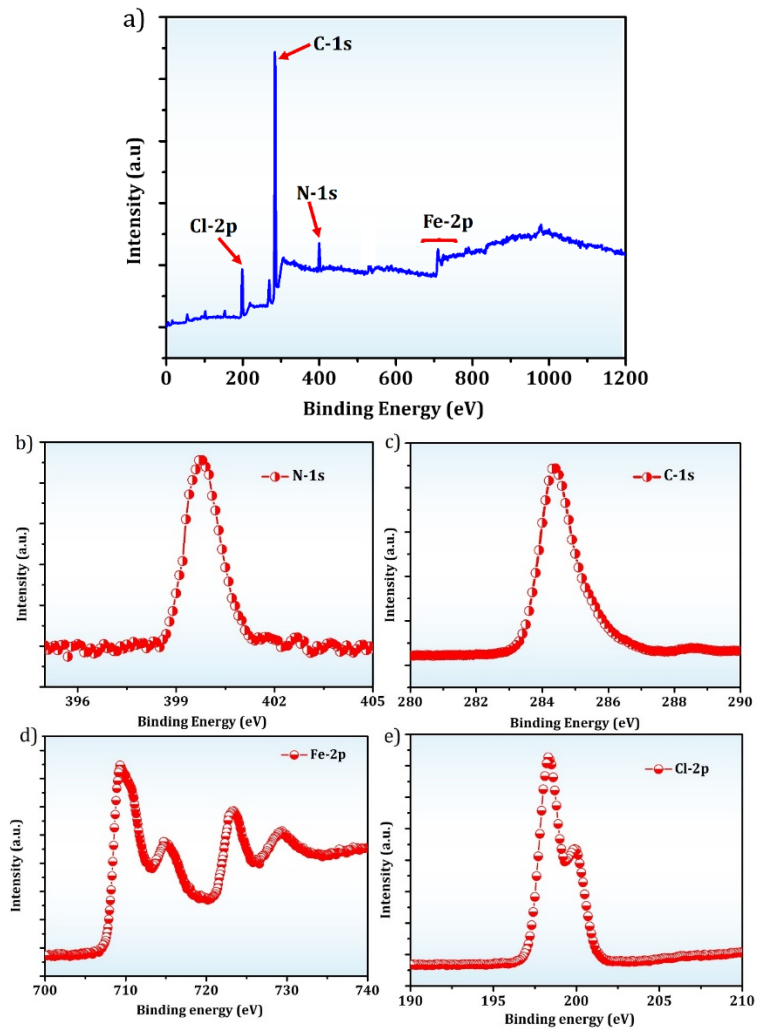

Figure S6. (a) Survey XPS spectrum of (pyz)$FeCl_2$. (b-e) High resolution XPS spectra of N 1s (b), C 1s (c), Fe 2p (d), and Cl 2p (e).

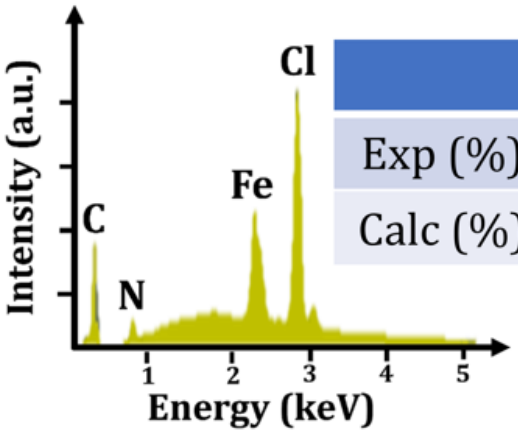

	C	N	Fe	Cl
Exp (%)	22.9	13.48	27.43	34.2
Calc (%)	23.2	13.53	27	34.28

Figure S7. EDS compositional analysis of (pyz)$FeCl_2$ microcrystals.

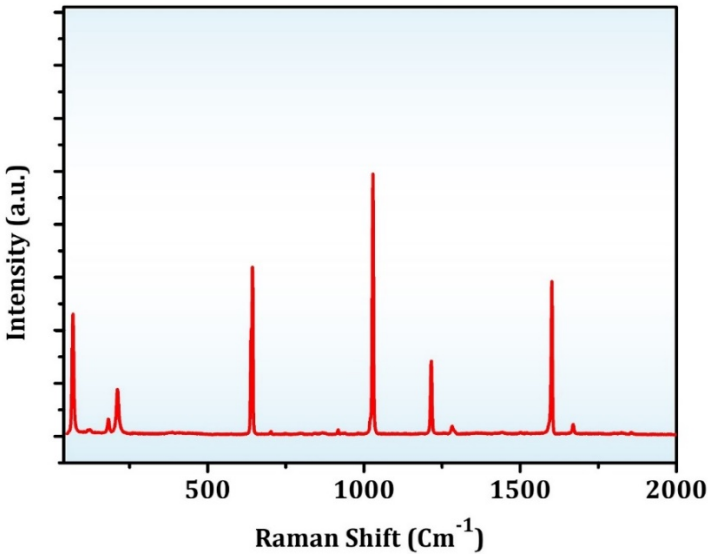

Figure S8. Raman spectra of (pyz)$FeCl_2$

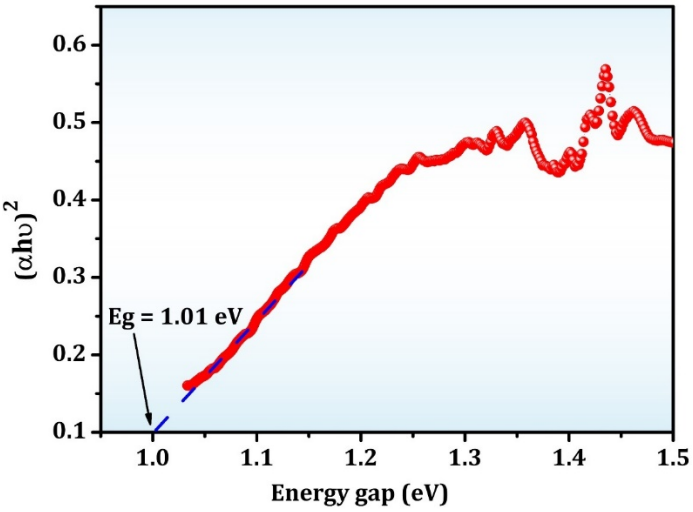

Figure S9. optical band gap (direct Tauc plot method) of (pyz)$FeCl_2$

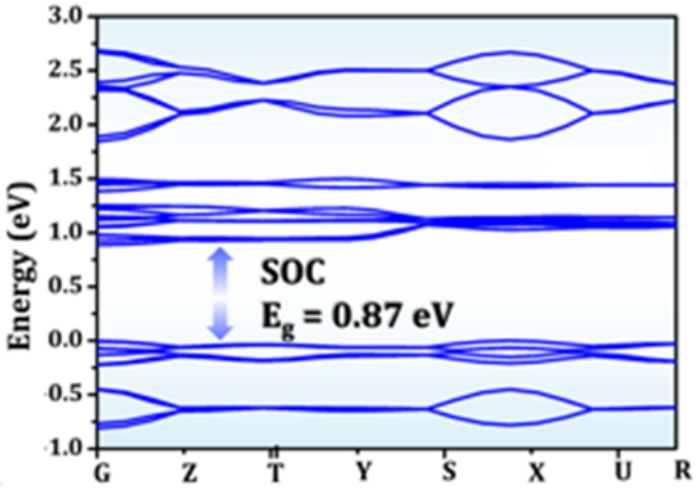

Figure S10. Electronic band structures calculated by DFT with spin–orbit coupling (SOC) of (pyz)$FeCl_2$

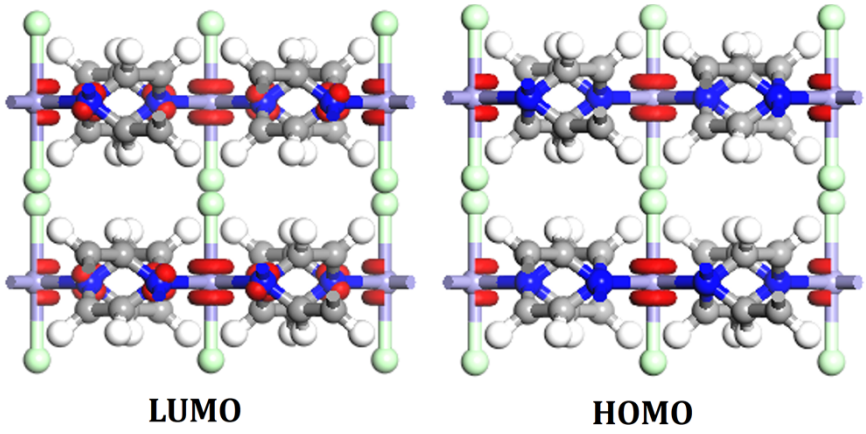

Figure S11. Frontier-state isosurfaces at the conduction-band muninum (LUMO) and Frontier state isosurfaces at the valence-band maximum (HOMO) (isovalue = 0.02 eV) of (pyz)$FeCl_2$ (Fe: Light Violet/ Cl: Light Green/ N: Bleu/ C: Grey/ H: White)

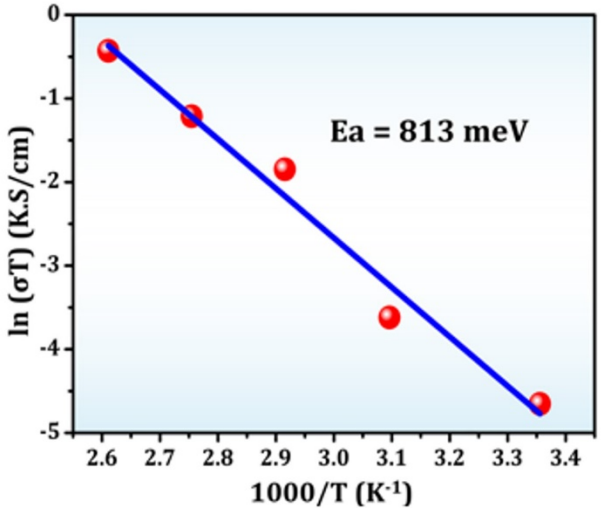

Figure S12. Arrhenius fit of ln(σT) vs. inverse temperature for (pyz)$FeCl_2$

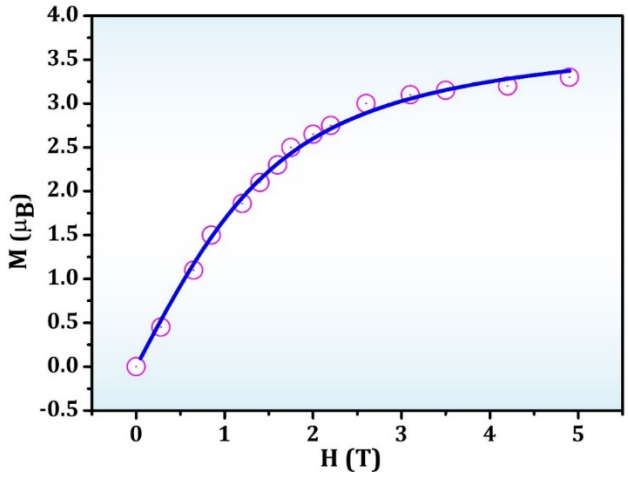

Figure S13. Field-Dependent Magnetization at 2 K for (pyz)$FeCl_2$. Purple line: model fit to magnetisation isotherm at 2K, $M(H) = M_s \tanh(H/H_0)$, with M_s = 3.59 ± 0.05 μB Fe^{-1} and H_0 = 1.8 ± 0.1 T

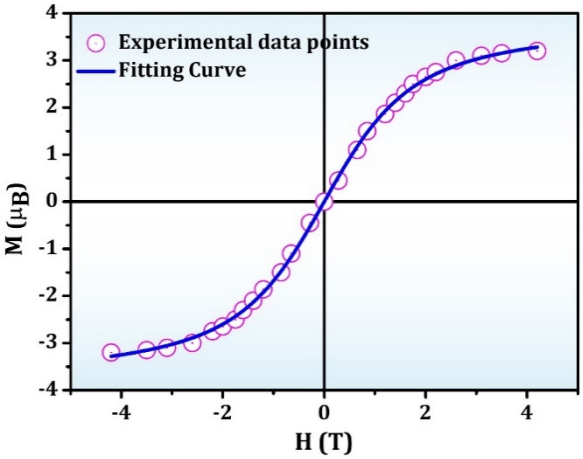

Figure S14. Magnetization vs Magnetic Field at 2 K for (pyz)$FeCl_2$. Purple line: model fit to your 2 K magnetisation isotherm, $M(H) = M_s \tanh(H/H_0)$, with M_s = 3.08 ± 0.05 μB Fe^{-1} and H_0 = 1.8 ± 0.1 T.

6. References

[S1] G. M. Sheldrick, A short history of *SHELX*, Acta Crystallogr. A., 2008, 64, 112-122.

[S2] P. Kubelka, Ein Beitrag Zur Optik Der Farbanstriche, Z. Technical Phys., 1931, 12, 593 -601

[S3] J. Tauc, Mater. Res. Bull., 1970, 5, 721 —729

[S4] F. E. M. O'BRIEN, J. Sci. Instrum. 1948, 25, 73–76

[S5] J. Hafner, J. Comput. Chem. 2008. 29, 2044-2078.

[S6] J.P. Perdew, K. Burke, M. Ernzerhof, [J]. Physical Review Letter. 1996, 77(18), 3865-3868.

[S7] D. M. Ceperley and B. J. Alder, Phys. Rev. Lett. 1980, 45, 566.

[S8] J. P. Perdew and A. Zunger, Phys. Rev. B: Condens. Matter Mater. Phys. 1981, 23, 5048

[S9] M.S. Lassoued, Y.C. Pang, Q.W. Li, X.K. Ding, B. Jiao, H. Dong, G.J. Zhou, S.J. Ding, Z.C. Zhang, Z.X. Wu, G.Y. Gou, Y.Z. Yin, J. Li, Y.Z. Zheng, Mater. Chem. Front, 2022, 6, 71-77.

[S10] J. K. Pious, A. Katre, C. Muthu, S. Chakraborty, S. Krishna, and C. Vijayakumar, Chem. Mater., 2019, 31, 1941−1945.

[S11] J-H. Qin, Y-D. Huang, Y. Zhao, X-G. Yang, F-F. Li, C. Wang, L.-F. Ma, Inorg. Chem., 2019, 58, 15013−15016.

[S12] X. Tian, Y. Zhang, R. Zheng, D. Wei, and J. Liu, Sustain. Energ. Fuels., 2020, 4, 2087-2113.

[S13] Y. Y. Chen, L. W. Tang, Y. Liu, T. Yang, L. Hua, X. Zeng, J. H. Luo, Z. H. Sun, J. Mater. Chem. C, 2023,11, 3981-3988.

[S14] J. C. Zhou, Y. L. Chu, J. Huang, ACS Appl. Mater. Interfaces., 2016, 8 (39), 25660-25666.

[S15] A. Dey, J. Ye, A. De, E. Debroye, S. K. Ha, E. Bladt, A. S. Kshirsagar, Z. Wang, J. Yin, Y. Wang, L. N.Quan, F. Yan, M. Gao, X. Li, J. Shamsi, T. Debnath, M. Cao, M. A. Scheel, S. Kumar, J. A. Steele, M. Gerhard, L. Chouhan, K. Xu, X-g. Wu, Y. Li, Y. Zhang, A. Dutta, C. Han, I. Vincon, A. L. Rogach, A. Nag, A. Samanta, B. A. Korgel, C-J. Shih, D. R. Gamelin, D. H. Son, H. Zeng, H. Zhong, H. Sun, H. V. Demir, I. G. Scheblykin, I. M Seró, J. K. Stolarczyk, J. Z. Zhang, J. Feldmann, J. Hofkens, J. M. Luther, J. P-Prieto, L. Li, L. Manna, M. I. Bodnarchuk, M. V. Kovalenko, M. B. J. Roeffaers, N. Pradhan, O.F. Mohammed, O. M. Bakr, P. Yang, P. M-Buschbaum, P V. Kamat, Q. Bao, Q. Zhang, R. Krahne, R. E. Galian, S. D. Stranks, S. Bals, V.

Biju, W. A. Tisdale, Y. Yan, R. L. Z. Hoye, and L. Polavarapu, ACS Nano., 2021, 15, 10775−10981.

[S16] X.L. Lin, B. Chen, Y.R. Huang, K.Y. Song, P.K. Zhou, L.L. Zong, H.H. Li , Z.R. Chen and R. Jiang, Inorg. Chem. Front, 2020, 7, 4477-4487.

[S17] L.M. Zhao, W.T. Zhang, K.Y. Song, Q.Q. Wu, Y. Li, H.H. Li and Z.R. Chen, Cryst Eng Comm, 2018, 20, 2245-2252.